Branching development of early post-implantation human embryonic-like tissues in 3D stem cell culture

Kejie Chen[1], Yi Zheng[1], Xufeng Xue[1], Yue Liu[1], Agnes M. Resto Irizarry[1], Huaijing Tang[1], and Jianping Fu[1,2,3] *

[1] Department of Mechanical Engineering, University of Michigan, Ann Arbor, MI, 48109, USA
[2] Department of Biomedical Engineering, University of Michigan, Ann Arbor, MI, 48109, USA
[3] Department of Cell & Developmental Biology, University of Michigan Medical School, Ann Arbor, MI, 48109, USA

Abstract

Human embryonic stem cells (hESCs) have the intrinsic capacity to self-organize and generate patterned tissues. *In vitro* models that coax hESCs to form embryonic-like structures by modulating physical environments and priming with chemical signals have become a powerful tool for dissecting the regulatory mechanisms underlying early human development. Here we present a 3D suspension culture system of hESCs that can generate post-implantation, pre-gastrulation embryonic-like tissues in an efficient and controllable manner. The efficiency of the development of asymmetric tissues, which mimic the post-implantation, pre-gastrulation amniotic sac, was about 50% in the 3D suspension culture. Quantitative imaging profiling and unsupervised trajectory analysis revealed that hESC aggregates first entered into a transitional stage expressing Brachyury (or T), before their development branched into different paths to develop into asymmetric embryonic-like tissues, amniotic-like tissues, and mesodermal-like tissues, respectively. Moreover, the branching developmental trajectory of embryonic-like structures was affected by the initial cell seeding density or cluster size of hESCs. A higher percentage of amniotic-like tissues was observed under a small initial cell seeding density of hESCs. Conversely, a large initial cell seeding density of hESCs promoted the development of mesodermal-like tissues. Intermediate cell seeding densities of hESCs in the 3D suspension culture promoted the development of asymmetric embryonic-like tissues. Our results suggest that hESCs have the intrinsic capability to sense the initial cell population size, which in turn regulates their differentiation and self-organization into different embryonic-like tissues. Our 3D suspension culture thus provides a promising experimental tool to study the interplay between tissue topology and self-organization and progressive embryonic development using *in vitro* hESC-based models.

1. Introduction

Embryonic development is a complex process regulated by multi-level signaling interactions and involves a series of morphological transformation [1-3]. Despite its fundamental and clinical importance, mechanisms underlying embryonic patterning and cell differentiation in human development remain incompletely understood, due to limited accessibility to human embryonic specimens and ethical restrictions [4, 5]. Recently, *in vitro* embryo models constructed from human embryonic stem cells (hESCs) are proposed as important alternatives of intact human embryos for studying human development [6-10]. hESCs reside in a developmental state similar to the post-implantation pluripotent epiblast cells [11-13]. As such, they have the potential to differentiate into the three definitive germ layer lineages. By culturing hESCs on a 2D micropatterned surface [14-16] or in a 3D environment [17-22], hESC-based, *in vitro* embryo models can recapitulate different aspects of the developments of some human embryonic structures. For example, an asymmetric embryonic-like sac structure, with amniotic cells at one side of the sac and pluripotent epiblast-like cells at the opposite side, enclosing a central lumen to mimic the pro-amniotic cavity, was successfully generated by embedding hESCs between two layers of native hydrogels [18]. This *in vitro* model, termed "post-implantation amniotic sac embryoid (PASE)", has been proposed as an experimental system to promote fundamental understanding of early post-implantation human development [18]. However, beyond phenomenological observations, limited mechanistic understanding has been generated due to suboptimal efficiency and controllability of the PASE model. Development of a more controllable and efficient method to generate the PASE would be an important step towards quantitative understanding of molecular and cellular mechanisms that drive human embryogenesis.

Most recent efforts have been directed towards developing bioengineering tools to provide controlled exogenous morphogen signals, such as BMP4 and WNT, to drive the formation of embryonic-like structures [14-22]. For example, Marfin et al. [15] and Zheng et al. [21] developed microfluidic devices to generate BMP4 signal gradients for cell fate patterning in 2D and 3D culture environments, respectively. However, although hESCs have prominent self-organizing properties and early developmental potential, few studies have so far recognized the importance of intrinsic factors in cell differentiation and embryonic pattern formation. Some previous studies on 2D hESC colonies [14, 23-25] and 3D embryoid bodies (EBs) [25-27] have shown that hESCs are able to sense the population contexts, such as the initial cell number in each cell colony and colony size, and change their differentiation accordingly. For example, large EBs support differentiation of neural-fated cells, whereas small EBs promote endoderm-fated cells, with both of them treated with the same differentiation medium [25]. However, since there is no reproducible spatial tissue organization in EBs, it is unclear whether the

population context affects patterned cellular structure developments in EBs. On a confined 2D surface, Warmflash et al. [14] observed the formation of an ordered array of three germ layers in response to BMP4 treatment. They further showed that spatial patterns of different cell types are controlled by the cell colony size. But the effect of cell population size on 3D tissue patterning and embryonic-like tissue development has not been well characterized.

Here we report a 3D suspension culture of hESCs with controllable input cell number in each cell colony. Using this 3D suspension culture, we studied developmental progression of hESC colonies to three types of post-implantation, pre-gastrulation embryonic-like tissues. Our data showed that hESC colonies in the 3D suspension culture followed a branching developmental trajectory and grew into asymmetric embryonic-like tissues (the PASE), amniotic-like tissues, and mesodermal-like tissues, respectively. The efficiency of generating asymmetric embryonic-like tissues was significantly higher than the previous method culturing hESCs within two layers of native hydrogels [18]. Next, we used an image-based tissue profiling pipeline to quantitatively characterize tissue morphogenetic properties and molecular features and studied their changes during the developments of the three embryonic-like tissues. We observed that the development of hESC colonies first entered a transitional stage where all cells expressed Brachyury (T box transcription factor, or T). Soon after, cells spontaneously broke symmetry and differentiated into two distinct cell fates, amniotic cells and mesodermal-like cells, in asymmetric embryonic-like tissues. On the contrary, all cells would follow a unique differentiation path in amniotic-like and mesodermal-like tissues, respectively. Furthermore, we observed that the branching tissue development was influenced by initial cell seeding density and thus initial cell number in each cell colony. A small initial cell seeding density supported the formation of amniotic-like tissues, whereas a large initial cell seeding density promoted the development of mesodermal-like tissues. Intermediate cell seeding densities of hESCs in the 3D suspension culture promoted the formation of asymmetric embryonic-like tissues, with an efficiency of about 50% in the 3D suspension culture. Together, the 3D suspension culture and the human embryonic-like tissues presented in this work could assist in mechanistic studies of the development of hESC-based synthetic human embryo models.

2. Materials and Methods

2.1 Fabrication of PDMS-based pyramidal devices

PDMS-based pyramidal devices were generated by replica-molding using AggreWell^{TM} 400 (StemCell Technologies; Figure S1). Briefly, as a primary mold, the AggreWell was cleaned with air plasma (Plasma Prep II; SPI Supplies) before being silanized with (tridecauoro-1,1,2,2-tetrahydrooctyl)-1-trichlorosilane vapor for 1 hour under vacuum. To make a template containing an array of pyramidal

posts, PDMS prepolymer was poured over the AggreWell plate. After degassing under vacuum and curing at 60°C for 12 hours, the template was peeled off from the AggreWell. The template was cut by an 8-mm biopsy punch to generate cylindrical secondary molds. The secondary molds were cleaned with air plasma before being silanized with (tridecauoro-1,1,2,2-tetrahydrooctyl)-1-trichlorosilane vapor for 1 hour under vacuum. To generate the final PDMS pyramidal wells, PDMS prepolymer was poured over the secondary mold. After degassing under vacuum and curing at 60° for 12 hours, the final device was peeled off from the secondary mold. Note that, for a PDMS pyramidal well, without any additional surface treatments, cells can aggregate at its bottom to form a spherical colony. In principle, the AggreWell can be replaced by other silicon molds to fabricate PDMS wells with prescribed sizes and geometries. For example, Hookway et al. [28] used silicon molds to fabricate PDMS and agarose wells to generate spheroids of hPSCs of different sizes.

2.2 Cell culture

H9 hESC line was maintained in a standard feeder-free culture using mTeSR1 medium (STEMCELL Technologies) and lactate dehydrogenase-elevating virus (LDEV)-free hESC-qualified reduced growth factor basement membrane matrix Geltrex™ (Thermo Fisher Scientific; derived from Engelbreth-HolmSwarm tumors similarly as Matrigel) per the manufacturer's instructions. H9 cells were used before P70.

2.3 Tissue generation and culturing

Low adhesive 96-well plates were prepared one day before experiments following a protocol reported previously [29]. Briefly, to prepare the hydrogel coating solution for low adhesive surfaces, 1.2 g poly-HEMA (Sigma Aldrich) was dissolved in 38 ml ethanol and 2 ml DI water at 37°C for 6 hours on a plate rotator. The hydrogel coating solution was then added to a 96-well plate (30 µl per well). The fully opened 96-well plate was placed in a tissue culture hood overnight to dry.

To generate spherical colonies of hESCs with defined initial cell numbers, hESC colonies in tissue culture dishes were dissociated with Accutase (Sigma Aldrich) at 37°C for 10 minutes, centrifuged and re-suspended in mTeSR1 medium containing 10 µM Y27632 (Tocris). Culture medium containing disassociated single hESCs was added to the pyramidal device and incubated for 6 hours. After 6 hours, spherical hESC colonies were transferred out of the device, centrifuged, and re-suspended in mTeSR1 medium supplemented with 5% Geltrex. Note that, a lower percentage of Geltrex does not support the growth of hESCs. A higher percentage of Geltrex could influence hESC behaviors as all, such as their

differentiation potential (data not shown). Culture medium with spherical hESC colonies was then added to the low adhesive 96-well plate for long-term culture.

2.4 Immunocytochemistry and microscopy

At different time points, hESC-derived, embryonic-like tissues were harvested from the low adhesive 96-well plate. These tissues were fixed in 4% paraformaldehyde (prepared in 1× PBS) for 3 hours and permeabilized in 0.1% SDS (sodium dodecylsulfate, dissolved in 1× PBS) solution for another 3 hours. Tissue samples were blocked in 4% donkey serum solution (Sigma Aldrich) at 4°C for 24 hours before incubation with a primary antibody solution at 4°C for another 24 hours. Samples were labeled with donkey-raised secondary antibodies (1:500 dilution) at 4°C for 24 hours. DAPI (Thermo Fisher Scientific) was used for counterstaining cell nuclei. Alexa fluor 488-conjugated wheat germ agglutinins (WGA; Thermo Fisher Scientific) was used as a pan-cell membrane marker. Primary antibodies and their sources and dilutions were provided in Table S1.

Images were acquired on an Olympus IX81 fluorescent microscope equipped with a CSU-X1 spinning-disc unit (YOKOGAWA) or a Nikon-A1 laser scanning confocal microscope (Nikon).

2.5 Image analysis pipeline

We quantified tissue properties, including morphological features and lineage marker expression, using an automatic image processing workflow for fluorescent confocal images [30]. The workflow contained two main steps: segmentation and feature extraction (Figure 2a). Segmentation provided a simplified representation of a multicellular tissue. Feature extraction provided quantifications of tissue morphological features and molecular marker intensities. Specifically, for tissue segmentation (Figure S2a), an intensity-based Watershed algorithm on a binary mask generated by Gaussian filter and median filter was applied to fluorescent images. To identify individual cells based on DAPI staining (Figure S2b), a shape-based Watershed algorithm, adopted from the python CellProfiler package [31], was used.

Fourteen morphological features were extracted from tissue segmentation and used to distinguish symmetric *vs.* asymmetric embryonic-like tissues. Specifically, an asymmetric embryonic-like tissue contained a thin amniotic epithelium at one side of the tissue and a thick, columnar cell layer at the opposite side. A symmetric embryonic-like tissue had a relatively uniform cell layer surrounding the central lumen (Figure 2a). Therefore, tissue thickness t_θ was introduced. As shown in Figure S2c, t_θ was defined as the tissue thickness at angle θ ($\theta \in [0, 2\pi]$) in a polar coordinate, where the center of the coordinate system was at the mass center of the lumenal cavity. Symmetry of a tissue was quantified by a thickness ratio r_t, where $r_t = \frac{\max(t_\theta)}{\min(t_\theta)}$. For a symmetric tissue, r_t was close to 1. For an asymmetric

tissue, r_t was much greater than 1. To quantify the size of a tissue, tissue area and equivalent tissue diameter were used. To quantify the roundness of a tissue, major axis length, minor axis length, and eccentricity of the tissue were calculated. Detailed definitions of the fourteen morphological features were listed in Table S2.

Thirteen lineage marker intensity features were extracted based on segmentation of cell nuclei. Specifically, the average intensities of GATA3, NANOG and T of a cell nucleus were calculated. When the average nucleus intensity of a marker, say GATA3, was two times greater than the background intensity, the cell was regarded as a GATA3+ cell. To quantify the distribution of different types of cells within a tissue, marker intensity gyration was introduced. For example, GATA3 gyration represented the distance between the mass center of GATA3+ cells and the mass center of the lumen. GATA3-T gyration was defined as the distance between the mass center of GATA3+ cells and the mass center of T+ cells. The definitions of lineage marker intensity features were listed in Table S2.

2.6 Multi-class support vector machine (SVM) classifier

To find the criteria of classifying asymmetric embryonic-like tissues, amniotic-like tissues and mesodermal-like tissues in an unbiased way, a linear multi-class SVM classifier is used. Specifically, at 65h, tissues can easily be distinguished based on their morphology and fluorescent marker intensity. Therefore, 30 images of asymmetric embryonic-like tissues, 30 images of amniotic-like tissues and 30 images of mesodermal-like tissues are manually selected. For i^{th} of the 90 tissue images, its normalized features, including the thickness ratio and GATA3+ cell ratio, are calculated using the image analysis pipeline, denoted as $\boldsymbol{x}_i$ ($i \in [1, 90]$). First, to find the criteria for classifying asymmetric and symmetric tissues, the label of image i, denoted as y_i, is set to 1 if it contains an asymmetric tissue and otherwise is set to 0. The cost function $L = \left[\frac{1}{90}\sum_{i=1}^{90}\max(0, 1 - y_i(\boldsymbol{w}^T\boldsymbol{x}_i + b))\right] + 0.1\|\boldsymbol{w}\|^2$ is minimized to get $\boldsymbol{w}_1$ and b_1. The SVM classifier $y = \boldsymbol{w}_1{}^T\boldsymbol{x} + b_1$, plotted in Figure 2(b), shows that whether the thickness ratio is larger than 4.4 is an unbiased criterion for distinguishing asymmetric and symmetric tissues. Next, to find the criteria for classifying amniotic-like and mesodermal-like tissues, in the 60 symmetric tissues, the label of image i ($i \in [1, 60]$) is set to 1 if it contains an amniotic-like tissue and otherwise is set to 0. Then, the cost function $L = \left[\frac{1}{60}\sum_{i=1}^{60}\max(0, 1 - y_i(\boldsymbol{w}^T\boldsymbol{x}_i + b))\right] + 0.1\|\boldsymbol{w}\|^2$ is minimized to get $\boldsymbol{w}_2$ and b_2. The SVM classifier $y = \boldsymbol{w}_2{}^T\boldsymbol{x} + b_2$ plotted in Figure 2(b) suggests that whether the GATA3+ cell ratio is larger than 0.5 is an unbiased criterion for classifying amniotic-like and mesodermal-like tissues when the thickness ratio is smaller than 4.4. The training of the SVM classifier is performed using python scikit-learn package [32]. RBF kernel with a parameter $\gamma = 0.1$ and one-vs-

one ('ovo') decision function were used. For the same type of tissues, tissue morphology and fluorescent marker intensity are not influenced by initial cell seeding density. Therefore, the SVM classifier is applied to quantify the percentages of the three types of tissues generated from small, intermediate and large cell seeding densities.

2.7 Trajectory inference

The dataset contained 27 morphological and lineage marker intensity features of N tissues ($N = 555$ for a low initial cell seeding density, $N = 1166$ for an intermediate initial cell seeding density, and $N = 965$ for a high initial cell seeding density). First, the dataset was normalized to zero mean and unit variance. Then, the similarity between any two tissue samples i and j ($i, j \in [1, N]$), defined as $c_{ij} = e^{-|\mathbf{x_i}-\mathbf{x_j}|^2/2\varepsilon}$, was calculated, where $\mathbf{x}_i$ was a vector of features of tissue i, and ε was a model parameter. $\varepsilon = 0.05$ in this study. Next, the tissue data points were organized in a way that data points of similar tissues were placed together, and distant data points were tissues having distinct properties. Specifically, eigendecomposition was applied to the similarity matrix $C = \{c_{ij}\}$. The first three eigenvectors, referred to as diffusion components (DCs), were used as new coordinates to display and visualize the dataset, and the new coordinate space is referred to as a diffusion map [33]. Note that, the newly defined coordinates (DCs) do not have a clear physical meaning. The coordinates were chosen when the structure inside the data, such as the branches, can be clearly separated and visualized. However, the structure of the dataset contained important biological information owing to the way the data points were organized. In this study, the structure represented gradual changes of tissue properties and suggested the dynamic developmental progression of tissues. We calculated the diffusion maps of the dataset that contained all the features or a part of the features. Features that can optimally distinct between asymmetric embryonic-like tissues, amniotic-like tissues and mesodermal-like tissues were selected. To infer a branching developmental trajectory, the python algorithm Wishbone [34] was adopted to order the tissue samples and identify branches. Wishbone is an algorithm originally developed to analyze single-cell RNA-sequencing data and infer lineage bifurcation of cell fates. Serra et al. [30] has applied Wishbone to study the bifurcating development of intestinal organoids. To use Wishbone for staining images of embryonic-like tissues, the first eight DCs were used as inputs into the Wishbone algorithm. A tissue fixed and stained at the earliest time point and located at the apex of the diffusion maps was chosen as the starting point. 150 waypoints were automatically or manually selected. Ordered tissue images along the developmental trajectory were plotted. To plot lineage marker expression along the trajectory, the trajectory was divided into 120 bins.

3. Results

3.1 Guided self-organization of pre-gastrulation embryonic-like tissues

To generate hESC colonies of a uniform size, disassociated single hESCs (5.4×10^4 cells/ml) were seeded into PDMS pyramidal wells in mTeSR1 medium supplemented with the ROCK inhibitor Y27632 (10 μM) to prevent dissociation-induced apoptosis of hESCs [35]. After formation of initial hESC colonies, hESC colonies were transferred out of the pyramidal well array and cultured in the low adhesive 96-well plate (Figure 1a&b). By modulating the initial cell seeding density, the number of cells inside a single pyramidal well was controlled precisely (Figure 1c), leading to the formation of spherical cell colonies with a uniform size that was dependent on the initial cell seeding density. After culturing for 20 h, a central lumen developed inside each cell aggregate, recapitulating the epithelialization and lumenogenesis of epiblast cells soon after implantation of the human blastocyst [17, 18, 21]. The monolayer of cells surrounding the central lumen expressed NANOG, suggesting that they were pluripotent epiblast-like cells (Figure 1d). After culturing for 55 h, three types of tissues with different morphologies and cell lineage compositions were observed (Figure 1e). The asymmetric embryonic-like tissues contained squamous GATA3+ cells at one pole of the tissues and columnar T+ cells at the opposite pole. GATA3 is an amniotic ectoderm marker [17, 18, 21], and T is one of the earliest markers of the gastrulation and mesoderm induction [36, 37]. T+ cells also expressed CDX2 (Figure S3), another marker of the amniotic ectoderm as well as of the posterior primitive streak [36, 38]. Therefore, the asymmetric tissues mimic the posterior end of the bipolar amnion-epiblast structure at the early gastrulation stage. The amniotic-like tissues contained only GATA3+ cells, whereas the mesodermal-like tissues contained only T+ cells. Notably, some T+ cells lost E-cadherin expression, particularly in mesodermal-like tissues, indicating the onset of the epithelial-mesenchymal transition (EMT) process (Figure S4). These T+ cells became loosely connected to mesodermal-like tissues before disseminating into the surrounding environment. These disseminating cells showed high expression of SNAI2 (Figure S5), a critical mediator of the EMT and gastrulation [18, 39]. In addition, in all the three tissue types, a few NANOG+ cells were observed. Importantly, these cells also expressed SOX17 (Figure S3), suggesting them as human primordial germ cell (PGC)-like cells [21, 37].

3.2 Image-based tissue profiling and classification

To monitor differentiation and self-organization of hESCs, the pre-gastrulation embryonic-like tissues were fixed and stained for three lineage markers (NANOG for epiblast, GATA3 for amniotic cells, and T for gastrulating mesodermal cells, respectively) at different time points, imaged at a high resolution,

and segmented using the automatic image analysis pipeline (see Materials and Methods). The morphological properties and lineage marker expression of embryonic-like tissues were profiled to acquire a multivariate feature set (Figure 2a).

Specifically, we generated hESC aggregates using an intermediate cell seeding density (5.4×10^4 cells/ml; corresponding to an average of 43 cells per pyramidal well as shown in Figure 1c) and quantified the percentages of different types of embryonic-like tissues over time. To distinguish symmetric and asymmetric tissues, we calculated the thickness ratio r_t of a tissue, defined as the maximum thickness over the minimum thickness of the cell layer surrounding the central lumen. Among symmetric tissues, the percentage of GATA3+ cells or the GATA3+ cell ratio was used to distinguish amniotic-like tissues from epiblast-like or mesodermal-like tissues. Based on the unbiased linear SVM classifier (see Materials and Methods), the criteria used to classify an asymmetric tissue was the thickness ratio $r_t > 4.4$. To identify an amniotic-like tissue, the GATA3+ cell ratio should be greater than 0.5 (Figure 2b). From analyzing the 1166 tissue images (Figure 2c), we observed that the asymmetric embryonic-like tissues appeared at 50 h. By 65 h, the percentage of the asymmetric tissue was greater than 55%, whereas the protocol developed by Shao et al. [18] only generated less than 10% asymmetric tissues. By 65 h, around 14% tissues were amniotic-like tissues, and the rest 30% tissues were mesodermal-like tissues.

We further analyzed distributions of tissue morphological properties and lineage marker expression at different time points. Tissue area and total cell number in the tissue increased exponentially over time (Figure 2d&e). By 65 h, at the middle cross-section of the tissue (the imaging plane), the mean tissue area reached $1.27 \times 10^4 \mu m^2$ and contained approximately 47 cells. The mean tissue diameter is around 150 μm (Figure S6b). The lumen area increased during the first 55 h and maintained at a similar level from 55 h to 65 h (Figure 2d). GATA3+ cells appeared at 55 h (Figure 2e), later than the onset of the development of the asymmetric tissue (50 h), suggesting that changes of cell shape occurred earlier than GATA3 expression in amniotic cells. At 65 h, the number of GATA3+ cells displayed a bimodal distribution (Figure 2e). The first peak of the distribution, with a greater mean value, represented a population of amniotic-like tissues that contained a high percentage of GATA3+ cells. The other peak, with a less mean value and fewer GATA3+ cells, represents asymmetric embryonic-like tissues and mesodermal-like tissues. The total cell number was proportional to tissue area for all time points (Figure 2f). Before 65 h, tissues that had a large tissue area tended to contain more GATA3+ cells. However, at 65 h, tissues had separated into two groups. One group of tissues contained a large number of GATA3+ cells and had an intermediate tissue area. The other group had few GATA3+ cells but were more likely to have a large tissue area (Figure 2g). The two groups of tissues can also be clearly visualized in the

scatter plot of tissue area against tissue thickness ratio. Tissues that had a large tissue area tended to be symmetric, whereas asymmetric tissues had relatively small tissue areas (Figure 2h).

3.3 Branching developmental trajectory

The development of embryonic-like tissues is a continuous, progressive process. However, tissue immunostaining protocols commonly used to examine tissue morphology and cell fate patterning prohibit continuously tracking progressive development of a single embryonic-like tissue over time. To overcome this difficulty and reveal temporal developmental dynamics, we applied our culture system to generate a large number of embryonic-like tissues developed from a similar initial stage. Given their asynchronous development, tissue samples acquired at multiple discrete time points in our system could cover almost all developmental stages at a high resolution. Therefore, applying computational algorithms to order all tissue samples based on their developmental progression and infer a developmental trajectory will provide insights about the hidden dynamics during the development of pre-gastrulation embryonic-like tissues.

Specifically, to understand how spherical epiblast-like tissues with uniform sizes developed into three distinct tissue types, we quantified phenotypic changes of these tissues and inferred a branching developmental trajectory using the imaging multidimensional feature space (See Materials and Methods). The diffusion maps (Figure 3a-c) of the 1166 tissues we examined showed that the development of embryonic-like tissues trifurcated into three distinct branches at around 50 h (Figure 3c). Tissues at 20 h and 40 h appeared at the trunk of the trajectory maps (Figure 3d&h). The green branch at 55 h and 65 h (Figure 3d) had a large tissue thickness ratio (Figure 3a), representing the development of asymmetric embryonic-like tissues. The red branch at 55 h and 65 h (Figure 3d) had a small tissue thickness ratio (Figure 3a) and a small GATA3+ cell ratio (Figure 3b), thus representing the development of mesodermal-like tissues. Bifurcation of asymmetric embryonic-like tissue and mesodermal-like tissue developments occurred at around 0.5 psuedotime (Figure 3e-g). Specifically, before bifurcation at around 0.5 psuedotime, all the tissues in the trunk shared similar properties, rapidly losing NANOG expression and increasing GATA3 expression, with the tissue thickness ratio remaining small. After bifurcation, in the asymmetric embryonic-like tissue branch, tissues increased the NANOG+ cell ratio, with GATA3 intensity and tissue thickness ratio becoming greater. In contrast, for the mesodermal-like tissue branch, GATA3 expression decreased, with NANOG+ cell ratio and tissue thickness ratio remaining small. The blue branch (Figure 3h) with a large GATA3+ cell ratio at 65 h (Figure 3b) represented the development of amniotic-like tissues. Following the bifurcating development of amniotic-like tissues and mesodermal-like tissues (Figure 3i-k), T intensity and tissue area increased and

GATA3+ cell ratio remained small in the trunk. After bifurcation, in the amniotic-like tissue branch, T intensity dropped and the GATA3+ cell ratio increased rapidly until around 0.8 psuedotime. During this time period, tissue area of the amniotic-like tissue remained at a similar level, suggesting that cells underwent amniotic differentiation instead of proliferation. After 0.8 psuedotime, changes of T intensity and GATA3+ cell ratio slowed down, and the growth of amniotic tissue area was re-established. In the mesodermal-like tissue branch, T intensity kept increasing and reached a maximal value before gradually decreasing. In the mesodermal-like tissue branch, the GATA3+ cell ratio always remained at a small value, while the tissue area kept increasing. In addition, besides the trifurcating tissue development, a few tissues located between the asymmetric and amniotic-like branches (Figure 3l), suggesting them in a transitional stage between the two tissue types. Indeed, Shao et al. [18] observe that some asymmetric embryonic-like tissues eventually grew into amniotic-like tissues, suggesting that T+ cells might maintain the potential to differentiate into GATA3+ amniotic cells. Growing from the trunk of the trajectory map (labeled in grey in Figure 3l), amniotic-like tissues distinguished themselves from the asymmetric tissues through a greater ratio of GATA3+ cells (Figure 3m). However, both tissue types shared many similar properties, including the percentage of NANOG+ cells (Figure 3n) and T expression (Figure 3o).

Overall, embryonic-like tissues obtained at a single time point are associated with different developmental stages and tissue types (Figure 4a). Based on the computation algorithm, we ordered these tissues and recapitulated their trifurcating developmental progression (Figure 4b). Following the three distinct developmental paths, fluorescent images of embryonic-like tissues were recorded and analyzed to understand their developmental hallmarks (Figure 4c-e). Specifically, all embryonic-like tissues lost NANOG expression and entered a transitional stage in which all cells expressed T. Next, in the asymmetric embryonic-like tissue branch, a local region of cells broke symmetry and differentiated into GATA3+ amniotic cells, with remaining cells at the opposite pole becoming T+ mesodermal-like cells. In the amniotic-like tissue branch, all cells lost T and became uniformly squamous, GATA3+ amniotic cells. Continuous development of the asymmetric tissue and amniotic tissue led to the squamous amniotic cells became even thinner. In the mesodermal-like tissues, T expression and cell adhesion were reduced, and loosely attached cells began migratory and disseminated into the surrounding environment.

3.4 Branching development influenced by initial cell number

To understand how the initial cell number in each hESC colony regulates the branching development of pre-gastrulation embryonic-like tissues, we changed the cell seeding density, leading to a varying

number of cells to cluster in a single pyramidal well. In this work, embryonic-like tissues grown from a small initial cell number (around 17 cells) and from a large initial cell number (around 87 cells) were further studied.

Under a small initial cell seeding condition (1.8×10^4 cells/ml; an average of 17 cells per cell colony as shown in Figure 1c), the average tissue area, lumen area, diameter and the number of cells in embryonic-like tissues increased over time (Figure 5b&c and Figure S6a). Compared to tissue growth, the lumenogenesis of embryonic-like tissues was somewhat delayed (Figure 5b). At 20 h, majority of cell colonies did not contain a central lumen (Figure 5b). The average number of T+ cells reached a maximum at around 50 h before gradually decreasing (Figure 5c). Based on the linear SVM classifier (Figure 2b), the majority of tissues grew into asymmetric embryonic-like and amniotic-like tissues under the small initial cell seeding condition (Figure 5d). At 65 h, 43.4% tissues were amniotic-like tissues, and 49.7% tissues were asymmetric embryonic-like tissues. For all tissues, we did not observe a strong correlation between tissue thickness ratio and tissue equivalent diameter (Figure 5e). Symmetric tissues at 40 h and 50 h displayed the highest T expression; in contrast, T expression in asymmetric tissues at 65 h was relatively low (Figure 5f). Moreover, given the plasticity of the asymmetric and amniotic-like tissues, we did not observe a clear bifurcating trajectory (Figure 5g), which was also supported by Figure 3l. However, based on the GATA3+ cell ratio and tissue thickness ratio, the two tissue types were still identified (Figure 5h), with the amniotic-like tissue containing a high percentage of GATA3+ cells and the asymmetric embryonic-like tissue having a large thickness ratio (Figure 5i). In addition, the NANOG expression decreased to 0 before 0.4 psuedotime due to a loss of pluripotency, and then returned to a low level after 0.7 psuedotime, likely due to the emergence of PGC-like cells in both types of tissues (Figure 5i).

Under a high initial cell seeding condition (9.0×10^4 cells/ml), the average initial cell number in each hESC colony was around 87 (Figure 1c). We observed that these large cell colonies mainly grew into asymmetric embryonic-like tissues and mesodermal-like tissues (Figure 6a&d). At 12 h, the average tissue area was already close to 0.56×10^4 μm^2. The mean tissue area increased rapidly over time and became more than 1.9×10^4 μm^2 at 60 h (Figure 6b), much greater than the mean tissue area at 65 h for the intermediate initial cell seeding condition (1.27×10^4 μm^2). However, the lumen area only increased to 0.54×10^4 μm^2 at 65 h, which was similar to the mean value 0.52×10^4 μm^2 for the intermediate initial cell seeding condition. This observation is likely because in mesodermal-like tissues, gastrulating cells migrated into the surrounding environment, which increased tissue size but did not affect the lumen area. The average tissue diameter is around 176 μm at 60 h (Figure S6b). The numbers of cells and T+ cells in mesodermal-like tissues increased over time (Figure 6c). GATA3+ cells appeared

to mainly exist in tissues whose diameters were relatively small at 60 h (Figure 6e). The percentage of NANOG+ cell decreased rapidly during the first 48 h. At 60 h, one group of tissues had relatively small tissue areas but a large NANOG+ cell ratio, while another group had large tissue areas and a small NANOG+ cell ratio (Figure 6f). From the diffusion maps and Wishbone trajectory (Figure 6g&h), the bifurcation between asymmetric embryonic-like tissue and mesodermal-like tissues occurred at around 48 h, correlating to around 0.5 psuedotime. After bifurcation, the T+ cell ratio and tissue area in the asymmetric embryonic-like tissue branch became smaller than those in the mesodermal-like tissue branch, whereas the tissue thickness ratio was greater in the asymmetric embryonic-like tissue branch than that of the mesodermal-like tissue branch.

4. Discussion

Many current stem cell-based embryo models, including our own post-implantation amniotic sac embryoid (PASE) model, lack efficiency and reproducibility required for mechanistic studies and robust data acquisition. As such, a continuous development and improvement of these embryoid systems is needed. Indeed, this work reports our recent effort in developing improved culture methods to achieve the development of asymmetric embryonic-like tissues, with an efficiency of about 50%, a significant improvement compared to our previous PASE protocol [18]. Nonetheless, to more specifically study amniotic-like tissues and mesodermal-like tissues, we can reverse back to our original PASE model and use either small or high initial cell seeding densities to achieve efficient generations of amniotic-like or mesodermal-like tissues, respectively.

The generation of a higher percentage of asymmetric embryonic-like tissues in this work can be mainly attributed to three factors. First, the initial tissue size is precisely controlled via pyramidal wells. Second, instead of directly seeding single hESCs in Geltrex matrix in the PASE model, hESCs are first allowed to aggregate in the mTeSR medium in pyramidal wells to form spheroids. These hESC spheroids are then transferred to Geltrex matrix and become exposed to exogenous biochemical and biomechanical signals. Thus, the method reported in this work leads to more uniform cellular responses in hESC colonies. Lastly, a simple homogeneous culturing environment with an optimal Geltrex concentration is provided in the 3D suspension culture. In addition, hESCs instead of human induced pluripotent stem cells (hiPSCs) are used in all the experiments, which might also influence the percentages of the three types of tissues. Though previous studies of PASE model show that hESCs and hiPSCs behave very similarly to form the asymmetric structure, it is important to compare in parallel the behaviors of the two cell types in our proposed system in the future study. Nonetheless, after controlling the initial colony size and optimizing the Geltrex-based extracellular matrix, three types of tissues were still observed

under various initial seeding cell densities. Using synthetic hydrogels with controllable biomechanical signals (including ECM stiffness) and ECM signaling peptides to provide hESC colonies a well-defined microenvironment might help further elucidate whether the branching development to multiple embryonic-like tissue types is an intrinsic property of hESCs caused by stochastic fluctuation of gene expressions and single-cell sensing of the population context, or otherwise is mediated by cellular sensing of extracellular biomechanical and biochemical signals. It is also possible that both mechanisms might be in play, to guide the robustness of embryonic development and patterning.

We observed that the progressive development of embryonic-like tissues from hESCs required cells to enter a transitional stage, in which hESCs expressed T before differentiating into amniotic-like cells or gastrulating mesodermal-like cells. Our results agree with single-cell transcriptome data recently reported for the gastrulating human embryo by Tyser et al. [40], in which the epiblast cells appear to express T during their transition to the nascent mesoderm and the amniotic ectoderm. Our results further suggested that hESCs differentiated into amniotic-like cells at an early transitional stage when T expression was relatively low, whereas their differentiation into mesodermal-like cells happened at a later stage with greater T expression (Figure 3i and Figure S7a). We further observed PGC-like cells (NANOG+/SOX17+) in the three embryonic-like tissues (Figure 1b and Figure S3), suggesting that PGC-like cells could be specified in both amniogenic and mesoderm induction environments [21, 41, 42]. The percentage of PGC-like cells was significantly higher in the presence of amniotic cells (Figure 3e and Figure S7b). Future efforts should be directed to apply our system to study PGC specification in amniotic-like tissues and mesodermal-like tissues.

It is not yet clear why the initial cell number could affect the developmental trajectories of embryonic-like tissues from hESCs. One possibility is that the population context might lead to unspecified microenvironmental effects that can change the physiological state and gene expression of hESCs. For example, previous studies have reported the impact of colony size on pluripotency maintenance of hESCs, through secretion of BMP antagonists (such as GDF3) by hESCs to support their self-renewal [24]. Therefore, adjusting the initial cell number in each cell colony could influence local concentrations of morphogens and inhibitors to control tissue responses and developments. Another interesting observation from this work is the delayed onset of lumenogenesis in hESC colonies grown from a small initial cell seeding density (Figure 5b). In the mouse, it has been shown that the apical-basal polarization at the onset of the lumenogenesis in the epiblast compartment is critical for the progressive development of the epiblast [43]. All in all, these data support the interplay between tissue topology and self-organization and progressive embryonic development.

5. Conclusion

In this work, we introduced a controllable culture method to generate human pre-gastrulation embryonic-like tissues, including asymmetric embryonic-like tissues, amniotic-like tissues, and mesodermal-like tissues, through self-organization and spontaneous symmetry breaking of hESC colonies. We applied an image process pipeline and an unsupervised trajectory inference algorithm to analyze immunostaining images obtained at discrete time points, and revealed the dynamic changes of tissue morphology and cell lineage marker expressions during the branching development of these embryonic-like tissues. Together, our culture system as well as the tissue analysis pipeline should have a great potential for advancing fundamental understanding of spontaneous symmetry breaking in the early post-implantation epiblast compartment.

6. Data availability

Data supporting the findings of this study are available within the article and its Supplementary Information files and from the corresponding author upon reasonable request.

7. Acknowledgements

A.M.R.I. is partially supported by the National Science Foundation Graduate Research Fellowship under grant no. DGE 1256260. This research is supported by the Michigan-Cambridge Collaboration Initiative, the University of Michigan Mcubed Fund, the 21st Century Jobs Trust Fund received through the Michigan Strategic Fund from the State of Michigan (Grant CASE-315037), the National Institutes of Health (R21 NS113518 and R21 HD100931), and the National Science Foundation (CMMI 1917304 and CBET 1901718).

References

[1] Harland, Richard M. "A new view of embryo development and regeneration." Science 360, no. 6392 (2018): 967-968.

[2] Shahbazi, Marta N., and Magdalena Zernicka-Goetz. "Deconstructing and reconstructing the mouse and human early embryo." Nature cell biology 20, no. 8 (2018): 878-887.

[3] Niakan, Kathy K., Jinnuo Han, Roger A. Pedersen, Carlos Simon, and Renee A. Reijo Pera. "Human pre-implantation embryo development." Development 139, no. 5 (2012): 829-841.

[4] Hyun, Insoo, Amy Wilkerson, and Josephine Johnston. "Embryology policy: Revisit the 14-day rule." Nature 533, no. 7602 (2016): 169-171.

[5] Pera, Martin F. "Human embryo research and the 14-day rule." Development 144, no. 11 (2017): 1923-1925.

[6] Shahbazi, Marta N., Eric D. Siggia, and Magdalena Zernicka-Goetz. "Self-organization of stem cells into embryos: a window on early mammalian development." Science 364, no. 6444 (2019): 948-951.

[7] Rossant, Janet, and Patrick PL Tam. "New insights into early human development: lessons for stem cell derivation and differentiation." Cell stem cell 20, no. 1 (2017): 18-28.

[8] Shao, Yue, and Jianping Fu. "Synthetic human embryology: towards a quantitative future." Current Opinion in Genetics & Development 63 (2020): 30-35.

[9] Rivron, Nicolas, Martin Pera, Janet Rossant, A. Martinez Arias, Magdalena Zernicka-Goetz, Jianping Fu, Susanne van den Brink et al. "Debate ethics of embryo models from stem cells." Nature 564, no. 7735 (2018): 183-185.

[10] Fu, Jianping, Aryeh Warmflash, and Matthias P. Lutolf. "Stem-cell-based embryo models for fundamental research and translation." Nature Materials (2020): 1-13.

[11] Nakamura, Tomonori, Ikuhiro Okamoto, Kotaro Sasaki, Yukihiro Yabuta, Chizuru Iwatani, Hideaki Tsuchiya, Yasunari Seita, Shinichiro Nakamura, Takuya Yamamoto, and Mitinori Saitou. "A developmental coordinate of pluripotency among mice, monkeys and humans." Nature 537, no. 7618 (2016): 57-62.

[12] Osafune, Kenji, Leslie Caron, Malgorzata Borowiak, Rita J. Martinez, Claire S. Fitz-Gerald, Yasunori Sato, Chad A. Cowan, Kenneth R. Chien, and Douglas A. Melton. "Marked differences in differentiation propensity among human embryonic stem cell lines." Nature biotechnology 26, no. 3 (2008): 313-315.

[13] Zoldan, Janet, Emmanouil D. Karagiannis, Christopher Y. Lee, Daniel G. Anderson, Robert Langer, and Shulamit Levenberg. "The influence of scaffold elasticity on germ layer specification of human embryonic stem cells." Biomaterials 32, no. 36 (2011): 9612-9621.

[14] Warmflash, Aryeh, Benoit Sorre, Fred Etoc, Eric D. Siggia, and Ali H. Brivanlou. "A method to recapitulate early embryonic spatial patterning in human embryonic stem cells." Nature methods 11, no. 8 (2014): 847-854.

[15] Manfrin, Andrea, Yoji Tabata, Eric R. Paquet, Ambroise R. Vuaridel, François R. Rivest, Felix Naef, and Matthias P. Lutolf. "Engineered signaling centers for the spatially controlled patterning of human pluripotent stem cells." Nature methods 16, no. 7 (2019): 640.

[16] Xue, Xufeng, Yubing Sun, Agnes M. Resto-Irizarry, Ye Yuan, Koh Meng Aw Yong, Yi Zheng, Shinuo Weng et al. "Mechanics-guided embryonic patterning of neuroectoderm tissue from human pluripotent stem cells." Nature materials 17, no. 7 (2018): 633-641.

[17] Shao, Yue, Kenichiro Taniguchi, Katherine Gurdziel, Ryan F. Townshend, Xufeng Xue, Koh Meng Aw Yong, Jianming Sang, Jason R. Spence, Deborah L. Gumucio, and Jianping Fu. "Self-organized amniogenesis by human pluripotent stem cells in a biomimetic implantation-like niche." Nature materials 16, no. 4 (2017): 419-425.

[18] Shao, Yue, Kenichiro Taniguchi, Ryan F. Townshend, Toshio Miki, Deborah L. Gumucio, and Jianping Fu. "A pluripotent stem cell-based model for post-implantation human amniotic sac development." Nature communications 8, no. 1 (2017): 1-15.

[19] Simunovic, Mijo, Jakob J. Metzger, Fred Etoc, Anna Yoney, Albert Ruzo, Iain Martyn, Gist Croft, Dong Shin You, Ali H. Brivanlou, and Eric D. Siggia. "A 3D model of a human epiblast reveals BMP4-driven symmetry breaking." Nature cell biology 21, no. 7 (2019): 900-910.

[20] Moris, Naomi, Kerim Anlas, Susanne C. van den Brink, Anna Alemany, Julia Schröder, Sabitri Ghimire, Tina Balayo, Alexander van Oudenaarden, and Alfonso Martinez Arias. "An in vitro model of early anteroposterior organization during human development." Nature (2020): 1-6.

[21] Zheng, Yi, Xufeng Xue, Yue Shao, Sicong Wang, Sajedeh Nasr Esfahani, Zida Li, Jonathon M. Muncie et al. "Controlled modelling of human epiblast and amnion development using stem cells." Nature 573, no. 7774 (2019): 421-425.

[22] Zheng, Y., X. Xue, A. M. Resto-Irizarry, Z. Li, Y. Shao, G. Zhao, and J. Fu. "Dorsal-ventral patterned neural cyst from human pluripotent stem cells in a neurogenic niche." Science advances 5, no. 12 (2019): eaax5933.

[23] Blin, Guillaume, Darren Wisniewski, Catherine Picart, Manuel Thery, Michel Puceat, and Sally Lowell. "Geometrical confinement controls the asymmetric patterning of brachyury in cultures of pluripotent cells." Development 145, no. 18 (2018): dev166025.

[24] Peerani, Raheem, Balaji M. Rao, Celine Bauwens, Ting Yin, Geoffrey A. Wood, Andras Nagy, Eugenia Kumacheva, and Peter W. Zandstra. "Niche-mediated control of human embryonic stem cell self‐renewal and differentiation." The EMBO journal 26, no. 22 (2007): 4744-4755.

[25] Bauwens, Celine Liu, Raheem Peerani, Sylvia Niebruegge, Kimberly A. Woodhouse, Eugenia Kumacheva, Mansoor Husain, and Peter W. Zandstra. "Control of human embryonic stem cell colony and aggregate size heterogeneity influences differentiation trajectories." Stem cells 26, no. 9 (2008): 2300-2310.

[26] Hwang, Yu-Shik, Bong Geun Chung, Daniel Ortmann, Nobuaki Hattori, Hannes-Christian Moeller, and Ali Khademhosseini. "Microwell-mediated control of embryoid body size regulates embryonic stem cell fate via differential expression of WNT5a and WNT11." Proceedings of the National Academy of Sciences 106, no. 40 (2009): 16978-16983.

[27] Mohr, Jeffrey C., Jianhua Zhang, Samira M. Azarin, Andrew G. Soerens, Juan J. de Pablo, James A. Thomson, Gary E. Lyons, Sean P. Palecek, and Timothy J. Kamp. "The microwell control of embryoid body size in order to regulate cardiac differentiation of human embryonic stem cells." Biomaterials 31, no. 7 (2010): 1885-1893.

[28] Hookway, Tracy A., Jessica C. Butts, Emily Lee, Hengli Tang, and Todd C. McDevitt. "Aggregate formation and suspension culture of human pluripotent stem cells and differentiated progeny." Methods 101 (2016): 11-20.

[29] Kuroda, Yasumasa, Shohei Wakao, Masaaki Kitada, Toru Murakami, Makoto Nojima, and Mari Dezawa. "Isolation, culture and evaluation of multilineage-differentiating stress-enduring (Muse) cells." Nature protocols 8, no. 7 (2013): 1391.

[30] Serra, Denise, Urs Mayr, Andrea Boni, Ilya Lukonin, Markus Rempfler, Ludivine Challet Meylan, Michael B. Stadler et al. "Self-organization and symmetry breaking in intestinal organoid development." Nature 569, no. 7754 (2019): 66-72.

[31] Carpenter, Anne E., Thouis R. Jones, Michael R. Lamprecht, Colin Clarke, In Han Kang, Ola Friman, David A. Guertin et al. "CellProfiler: image analysis software for identifying and quantifying cell phenotypes." Genome biology 7, no. 10 (2006): R100.

[32] Pedregosa, Fabian, Gaël Varoquaux, Alexandre Gramfort, Vincent Michel, Bertrand Thirion, Olivier Grisel, Mathieu Blondel et al. "Scikit-learn: Machine learning in Python." the Journal of machine Learning research 12 (2011): 2825-2830.

[33] Moffat, Bradford A., Thomas L. Chenevert, Theodore S. Lawrence, Charles R. Meyer, Timothy D. Johnson, Qian Dong, Christina Tsien et al. "Functional diffusion map: a noninvasive MRI biomarker for

early stratification of clinical brain tumor response." Proceedings of the national academy of sciences 102, no. 15 (2005): 5524-5529.

[34] Setty, Manu, Michelle D. Tadmor, Shlomit Reich-Zeliger, Omer Angel, Tomer Meir Salame, Pooja Kathail, Kristy Choi, Sean Bendall, Nir Friedman, and Dana Pe'er. "Wishbone identifies bifurcating developmental trajectories from single-cell data." Nature biotechnology 34, no. 6 (2016): 637-645.

[35] Watanabe, Kiichi, Morio Ueno, Daisuke Kamiya, Ayaka Nishiyama, Michiru Matsumura, Takafumi Wataya, Jun B. Takahashi et al. "A ROCK inhibitor permits survival of dissociated human embryonic stem cells." Nature biotechnology 25, no. 6 (2007): 681-686.

[36] Bernardo, Andreia S., Tiago Faial, Lucy Gardner, Kathy K. Niakan, Daniel Ortmann, Claire E. Senner, Elizabeth M. Callery et al. "BRACHYURY and CDX2 mediate BMP-induced differentiation of human and mouse pluripotent stem cells into embryonic and extraembryonic lineages." Cell stem cell 9, no. 2 (2011): 144-155.

[37] Irie, Naoko, Leehee Weinberger, Walfred WC Tang, Toshihiro Kobayashi, Sergey Viukov, Yair S. Manor, Sabine Dietmann, Jacob H. Hanna, and M. Azim Surani. "SOX17 is a critical specifier of human primordial germ cell fate." Cell 160, no. 1-2 (2015): 253-268.

[38] Amin, Shilu, Roel Neijts, Salvatore Simmini, Carina van Rooijen, Sander C. Tan, Lennart Kester, Alexander van Oudenaarden, Menno P. Creyghton, and Jacqueline Deschamps. "Cdx and T brachyury co-activate growth signaling in the embryonic axial progenitor niche." Cell reports 17, no. 12 (2016): 3165-3177.

[39] Carver, Ethan A., Rulang Jiang, Yu Lan, Kathleen F. Oram, and Thomas Gridley. "The mouse snail gene encodes a key regulator of the epithelial-mesenchymal transition." Molecular and cellular biology 21, no. 23 (2001): 8184-8188.

[40] Tyser, Richard CV, Elmir Mahammadov, Shota Nakanoh, Ludovic Vallier, Antonio Scialdone, and Shankar Srinivas. "A spatially resolved single cell atlas of human gastrulation." bioRxiv (2020).

[41] Chen, Di, Na Sun, Lei Hou, Rachel Kim, Jared Faith, Marianna Aslanyan, Yu Tao et al. "Human primordial germ cells are specified from lineage-primed progenitors." Cell reports 29, no. 13 (2019): 4568-4582.

[42] Sasaki, Kotaro, Shihori Yokobayashi, Tomonori Nakamura, Ikuhiro Okamoto, Yukihiro Yabuta, Kazuki Kurimoto, Hiroshi Ohta et al. "Robust in vitro induction of human germ cell fate from pluripotent stem cells." Cell stem cell 17, no. 2 (2015): 178-194.

[43] Zhang, Zhechun, Steven Zwick, Ethan Loew, Joshua S. Grimley, and Sharad Ramanathan. "Mouse embryo geometry drives formation of robust signaling gradients through receptor localization." Nature communications 10, no. 1 (2019): 1-14.

Figures with their captions

Figure 1

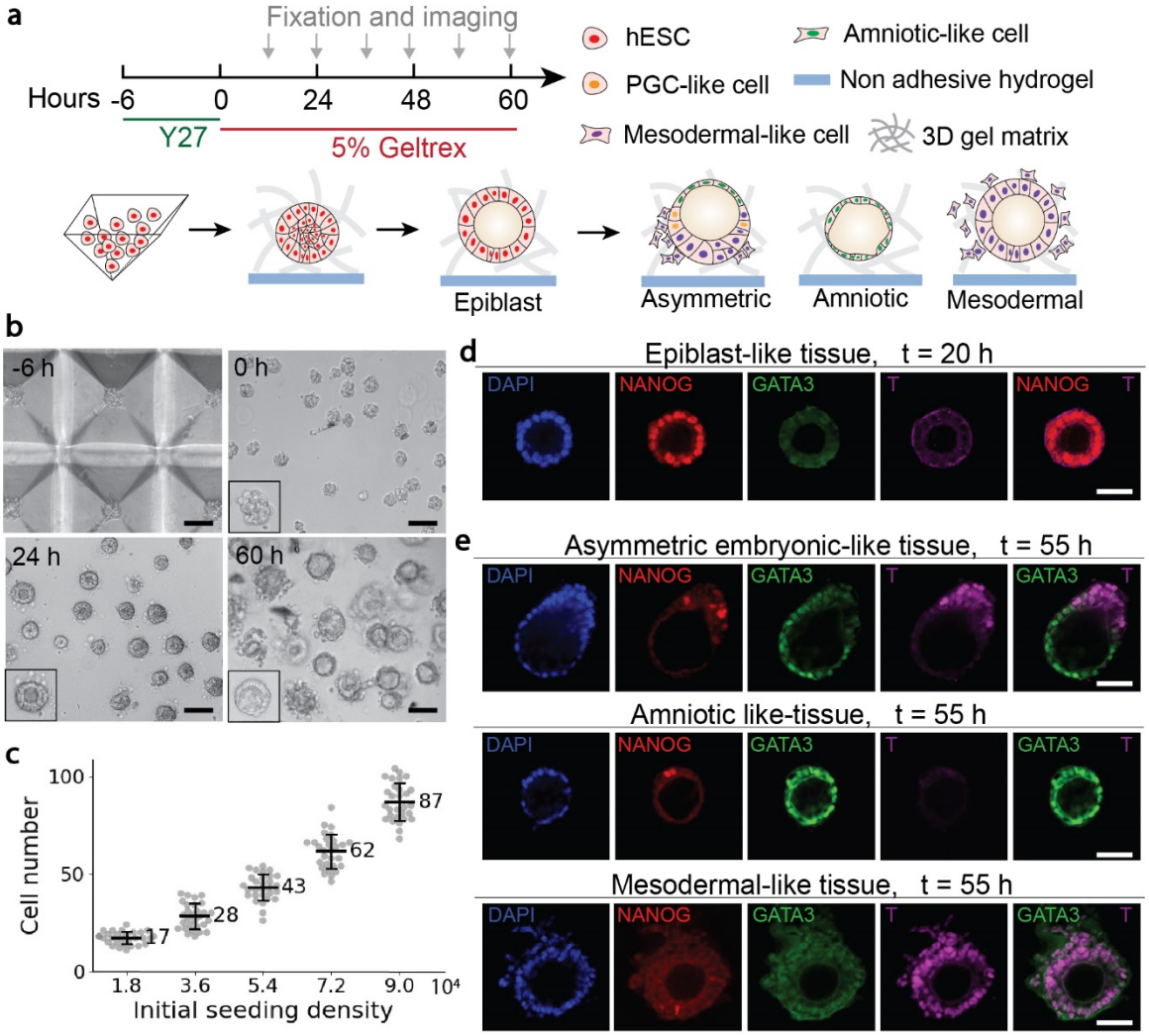

Figure 1. Guided self-organization of human pre-gastrulation embryonic-like tissues. a, Schematics of generating and long-time culturing three types of tissues from hESCs, including asymmetric embryonic-like tissues, amniotic-like tissues, and mesodermal-like tissues. **b**, Representative bright-field images of cells in the pyramid well array and tissues in the 3D gel matrix at different time points as indicated. Scale bars, 100 μm. **c**, Number of cells inside a single pyramidal well as a function of the initial cell seeding density. **d**, Representative confocal images of the epiblast-like tissues at 20 h stained for DAPI, NANOG, GATA3 and T. Scale bar, 50 μm. **e**, Representative confocal images of the three types of embryonic-like tissues at 55 h stained for DAPI, NANOG, GATA3 and T as indicated. Scale bars, 50 μm.

Figure 2

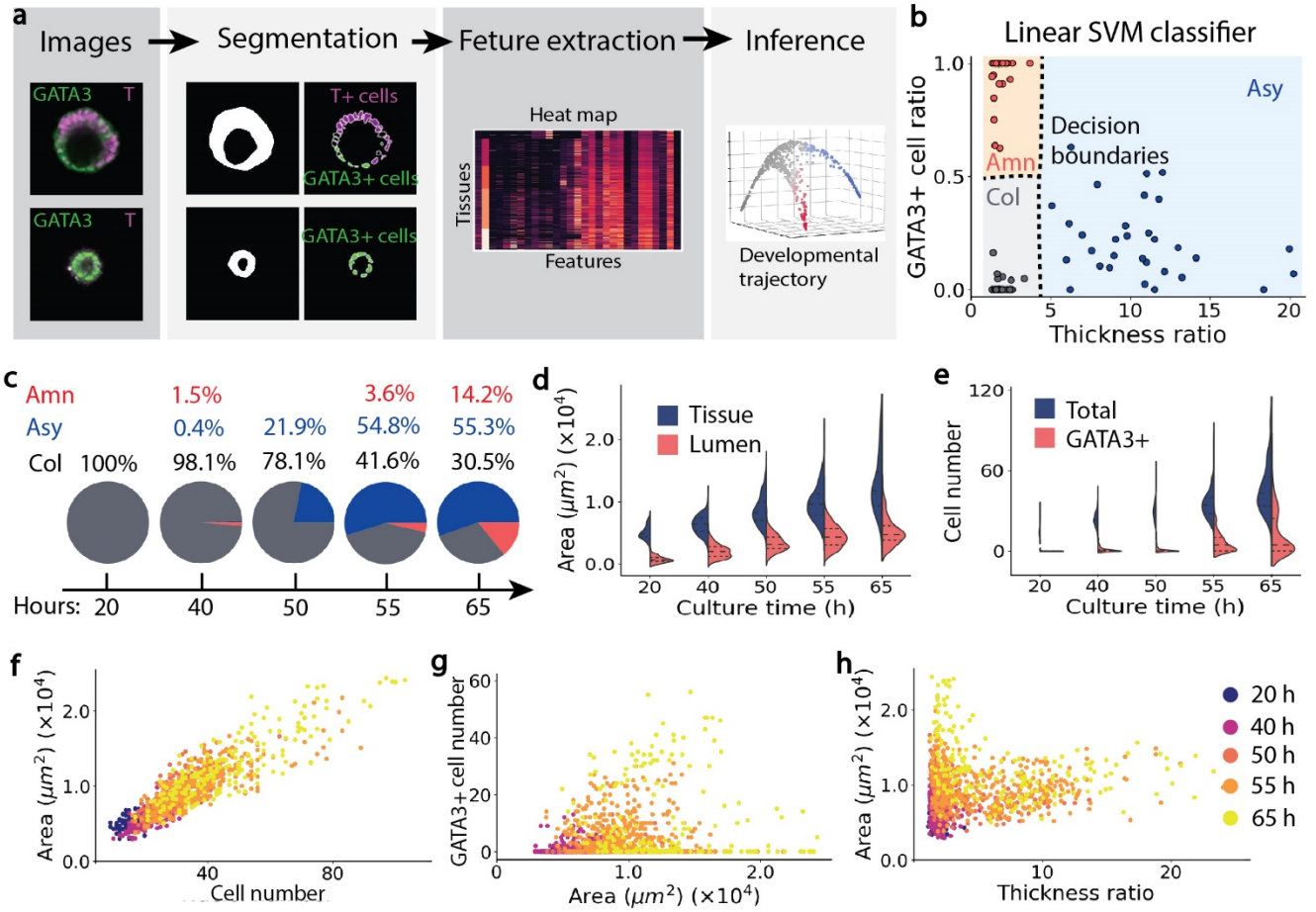

Figure 2. Properties of tissues grown from an intermediate cell seeding density ($n = 1166$). a, Schematics of image-based tissue profiling, which includes segmentation and feature extraction, and unsupervised trajectory inference. **b**, Linear multi-class SVM classifier for automatically distinguishing columnar (col), amniotic-like (amn) and asymmetric (asy) tissues. Dashed lines represent decision boundaries. **c**, Percentages of three types of tissues over time. **d**, Tissue and lumen area over culture time. **e**, Total cell number and GATA3+ cell number over culture time. **f**, Tissue area plotted against the number of cells contained in each tissue. **g**, Number of GATA3+ cells plotted against tissue area. **h**, Tissue area plotted against tissue thickness ratio. Color-coding in **f-h** denotes culture time of tissues.

Figure 3

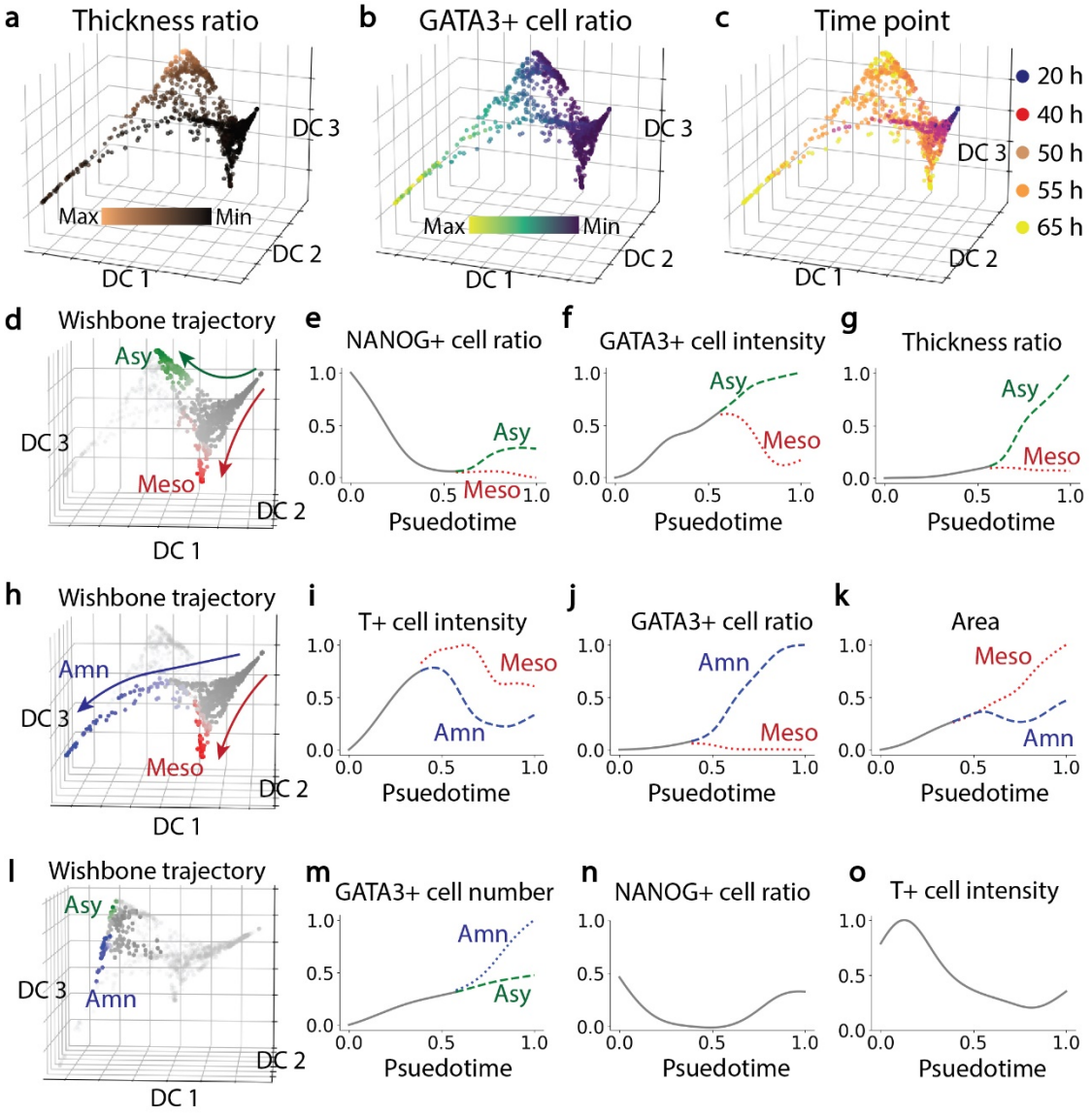

Figure 3. Developmental trajectories of tissues grown from an intermediate initial cell seeding density (n = 1166). a-c, Diffusion maps showing the trifurcating development of tissues. Color-coding denotes thickness ratio, GATA3+ cell ratio and culture time as indicated. **d**, Bifurcating trajectory of asymmetric embryonic-like tissues and mesodermal-like tissues. Color-coding denotes trunk and branch points. **e-g**, NANOG+ cell ratio, GATA3+ cell intensity and tissue thickness ratio as a function of pseudotime of tissue development. **h**, Bifurcating trajectory of amniotic-like tissues and mesodermal-like tissues. **i-k**, T+ cell intensity, GATA3+ cell ratio and tissue area as a function of pseudotime of tissue development. **l**, Intermediate states between asymmetric and amniotic branches. **m-o**, GATA3+ cell number, NANOG+ cell ratio and T+ cell intensity as a function of pseudotime of tissue development.

Figure 4

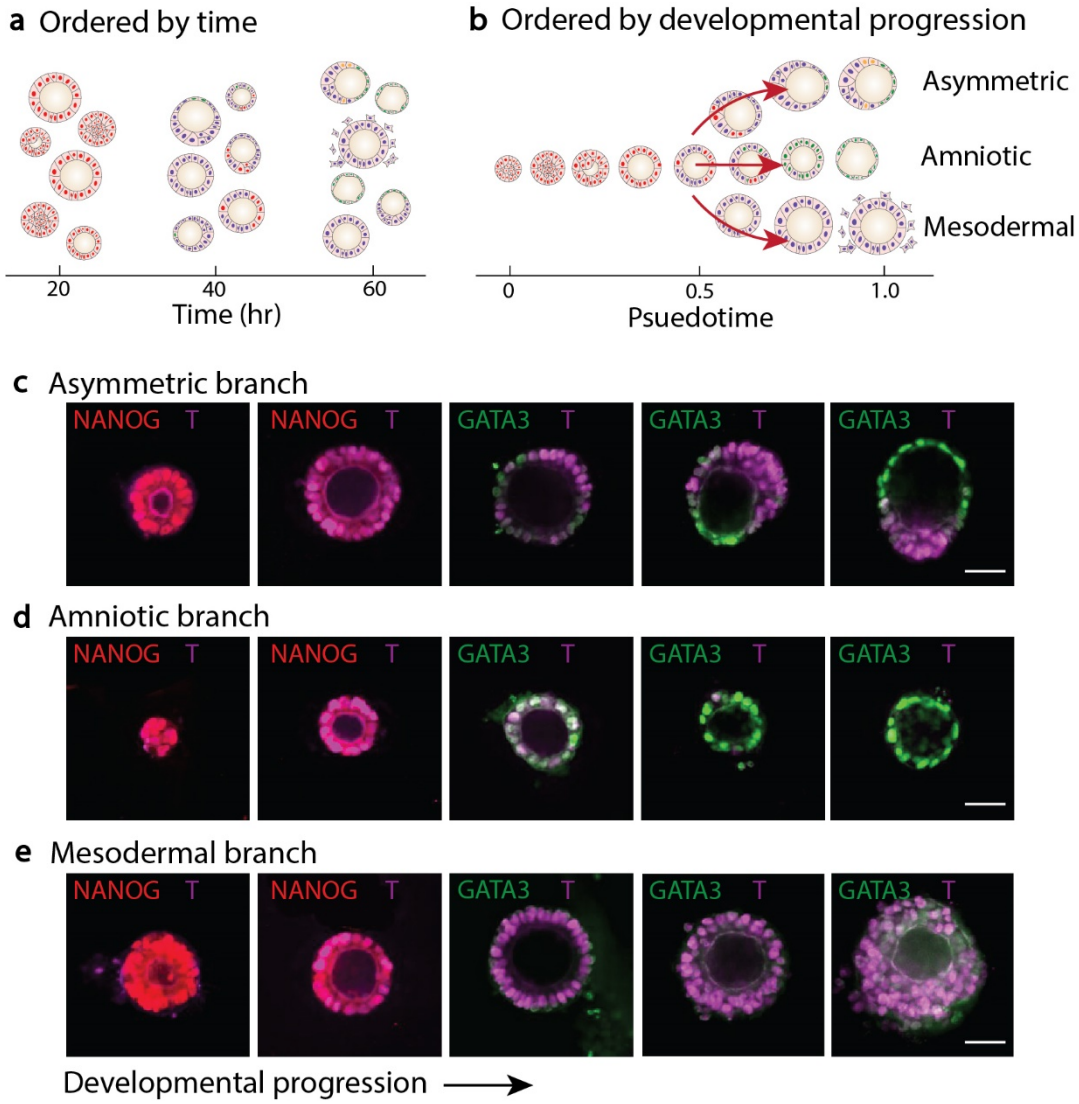

Figure 4. Progression of tissue development. a, Heterogeneous tissue morphology and cell lineage composition ordered by real time. **b**, Pseudotime ordering and trifurcating development. **c**, Representative images of tissues growing along the asymmetric branch. **d**, Representative images of tissues growing along the amniotic branch. **e**, Representative images of tissues growing along the mesodermal branch. Scale bars, 50 μm.

Figure 5

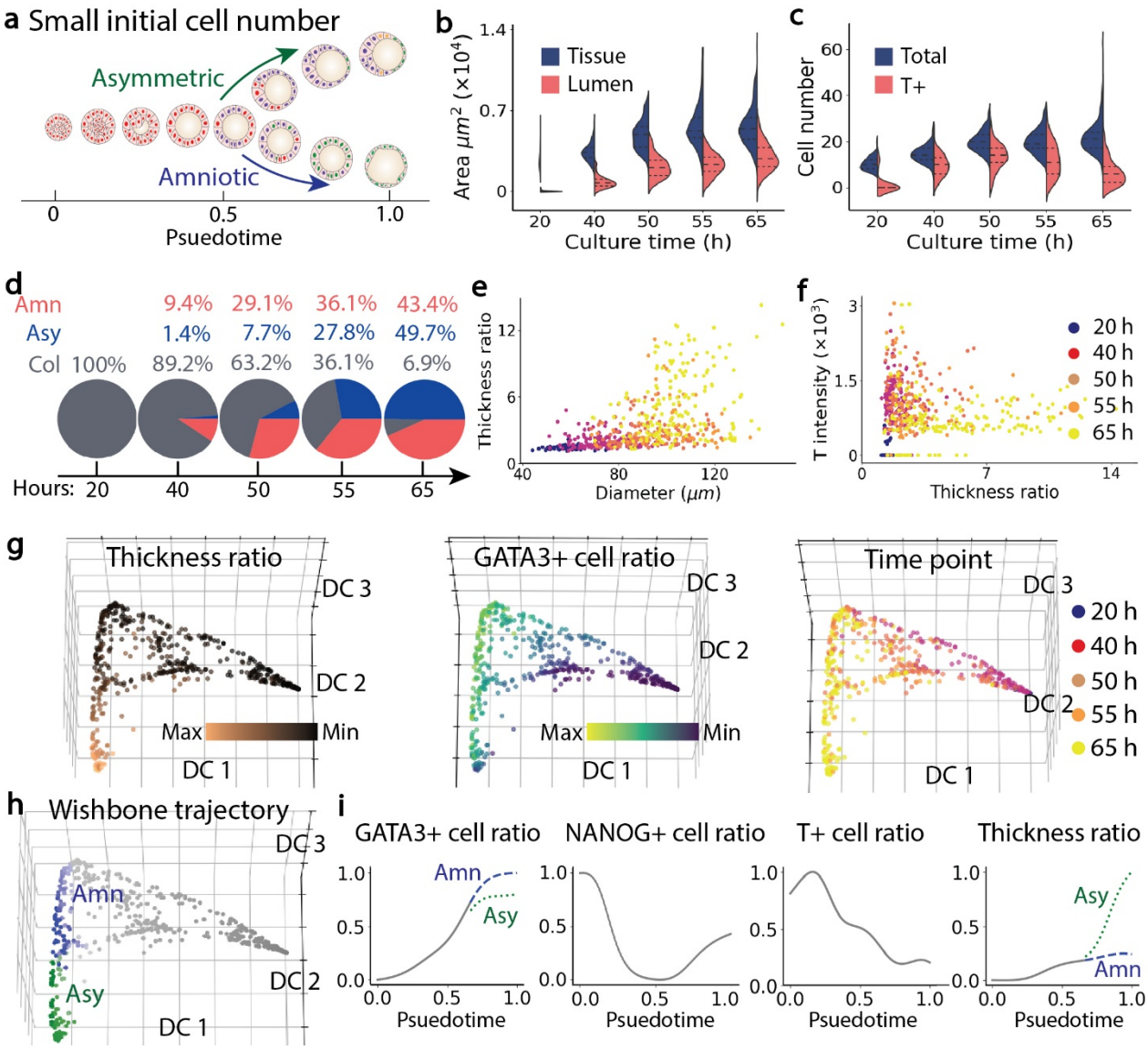

Figure 5. Properties and developmental trajectories of tissues grown from a small initial cell seeding density ($n = 555$). a, Schematics of bifurcating tissue development. **b**, Tissue area and lumen area as a function of culture time. **c**, Total cell number and T+ cell number as a function of culture time. **d**, Percentages of three types of tissues over time. **e**, Tissue thickness ratio plotted against tissue equivalent diameter. **f**, T+ cell intensity plotted against tissue thickness ratio. Color-coding in **e** and **f** denotes culture time. **g**, Diffusion maps of tissues. Color-coding denotes tissue thickness ratio, GATA3+ cell ratio and culture time as indicated. **h**, Bifurcating trajectory of amniotic-like and asymmetric tissues. **i**, GATA3+ cell ratio, NANOG+ cell ratio, T+ cell ratio and thickness ratio as a function of psuedotime of tissue development.

Figure 6

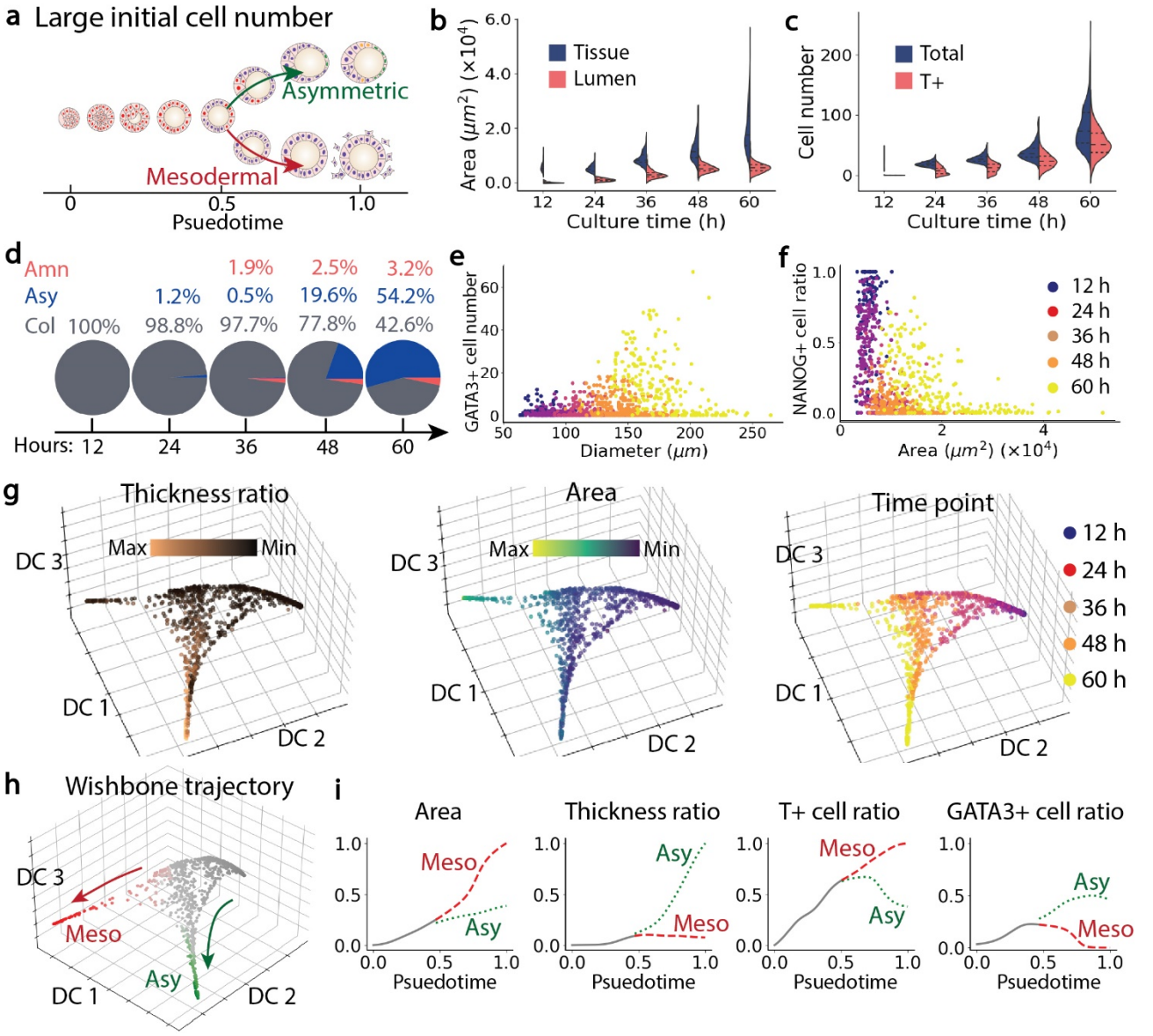

Figure 6. Properties and developmental trajectories of tissues grown from a large initial cell seeding density ($n = 965$). **a**, Schematics of bifurcating tissue development. **b**, Tissue area and lumen area over culture time. **c**, Total cell number and T+ cell number over culture time. **d**, Percentages of three types of tissues over time. **e**, GATA3+ cell number plotted against tissue equivalent diameter. **f**, NANOG+ cell ratio plotted against tissue area. Color-coding in **e** and **f** denotes culture time. **g**, Diffusion maps of tissues. Color-coding denotes tissue thickness ratio, area and culture time. **h**, Bifurcating trajectory of asymmetric and mesodermal-like tissues. **i**, T+ cell ratio, tissue area, and tissue thickness ratio as a function of psuedotime of tissue development.